In-Plane Anisotropic and Ultra-Low Loss Polaritons in a Natural van der Waals Crystal

Weiliang Ma,[1] Pablo Alonso-González,[2*] Shaojuan Li,[1] Alexey Y. Nikitin,[3,8] Jian Yuan,[1] Javier Martín-Sánchez,[2] Javier Taboada-Gutiérrez,[2] Iban Amenabar,[4] Peining Li,[4] Saül Vélez,[4,5] Christopher Tollan,[4] Zhigao Dai,[6] Yupeng Zhang,[6] Sharath Sriram,[7] Kourosh Kalantar-zadeh,[7] Shuit-Tong Lee,[1] Rainer Hillenbrand,[4,8*] Qiaoliang Bao[1,6*]

[1]Institute of Functional Nano and Soft Material (FUNSOM), Jiangsu Key Laboratory for Carbon-Cased Functional Materials and Devices, and Collaborative Innovation Center of Suzhou Nano Science and Technology, Soochow University, Suzhou 215123, China
[2]Departamento de Física, Universidad de Oviedo, 33007 Oviedo, Spain
[3]Donostia International Physics Center (DIPC), 20018 San Sebastián, Spain
[4]CIC nanoGUNE, 20018 San Sebastian, Spain
[5]Department of Materials, ETH Zürich, 8093 Zürich, Switzerland
[6]Department of Materials Science and Engineering, and ARC Centre of Excellence in Future Low-Energy Electronics Technologies (FLEET), Monash University, Clayton, Victoria 3800, Australia
[7]School of Engineering and the Micro Nano Research Facility, RMIT University, Melbourne, Australia
[8]IKERBASQUE, Basque Foundation for Science, 48011 Bilbao, Spain

*Corresponding author. E-mail: (P.A.G.) pabloalonso@uniovi.es; (R.H.) r.hillenbrand@nanogune.eu; (Q.B.) qiaoliang.bao@monash.edu
**W. Ma, P. Alonso-González and S. Li contributed equally to this work.

Polaritons – hybrid light-matter excitations – play a crucial role in fundamental and applied sciences, as they enable nanoscale control of light. Particularly large polariton confinements and long lifetimes can be found in graphene and van der Waals (vdW) materials[1,2]. Intriguingly, these polaritons can be tuned by electric fields[3,4] or by the material thickness [5], establishing a unique basis for manifold applications including nanolasers[6], tunable infrared and terahertz detectors[7], and molecular sensors[8].

Recently, polaritons with anisotropic propagation along the surface of vdW materials have been predicted, owing to in-plane anisotropic structural and electronic properties[9]. Elliptic and hyperbolic in-plane polariton dispersion can be expected (*e.g.*, plasmon polaritons in black phosphorus), the latter leading to an enhanced density of optical states and ray-like directional propagation along the surface. However, their observation in natural materials has so far remained elusive.

Here, we show the first images of anisotropic polariton propagation along the surface of a natural vdW material. By infrared nano-imaging and nano-spectroscopy of semiconducting α-MoO_3 flakes and disks we verify phonon polaritons with elliptic and hyperbolic in-plane dispersion, and with wavelengths (up to 60 times smaller than the corresponding photon wavelengths) being comparable to that of graphene plasmon and boron nitride phonon polaritons[3-5]. From the signal oscillations in the real-space images we measured record-high polariton amplitude lifetimes of 8 ps, which are more than one order of magnitude larger than that of graphene plasmons at room temperature[10] and a factor of about four larger than the best values reported for phonon polaritons in isotopically engineered boron nitride[11] and graphene plasmons at low temperature[12].

In-plane anisotropic and ultra-low loss polaritons in vdW materials could be applied for directional strong light-matter interactions, nanoscale directional energy transfer and integrated flat optics for applications ranging from bio-sensing to quantum nanophotonics.

(292 words)

Anisotropic optical materials exhibit numerous distinctive and non-intuitive optical phenomena such as negative refraction[13], hyper-lensing[14], wave-guiding[15] and enhanced quantum radiation[16], which have been demonstrated typically with artificial hyperbolic metamaterials. However, further progress is limited by optical losses and the complexity of metamaterial fabrication[17].
The recent emergence of low-loss van der Waals (vdW) materials opens the door for achieving anisotropic optical phenomena naturally, since their layered crystal structure leads to an intrinsic and strong out-of-plane (perpendicular to the layers) optical anisotropy[5,18]. A prominent example are hyperbolic phonon polaritons (PhPs) – infrared light coupled to lattice vibrations in layered polar materials - in hexagonal boron nitride (*h*-BN), which exhibit long lifetimes[11], ultra-slow propagation[19], and hyper-lensing effects[20,21]. Interestingly, when the layers of a vdW material are anisotropic (*i.e.*, when the permittivities along orthogonal in-plane directions are different), the polaritons are expected to propagate along the layers with an in-plane anisotropic dispersion[9]. In case that the permittivities are different but of the same sign, the polaritons possess an elliptic in-plane dispersion, where the iso-frequency contours (slices in two-dimensional (2D) wavevector space (k_x, k_y) of constant frequency ω) describe ellipsoids. When the signs are different, the polaritons possess an in-plane hyperbolic dispersion, where the iso-frequency contours are open hyberboloids[22]. Only recently, phonon polaritons with in-plane hyperbolic dispersion have been demonstrated by fabricating an artificial metamaterial out of *h*-BN flakes[23].

Excitingly, theory predicts polaritons with both in-plane anisotropies even for natural materials (without any nanostructuring), which exhibit an in-plane anisotropy of their electronic or structural properties; for example, hyperbolic plasmons - light coupled to free carriers - in black phosphorus[9] or in Weyl semimetals[24]. While being expected to provide novel fundamental insights into exotic material properties (*i.e.*, nonreciprocal Purcell enhancement[24]), they also bear exciting application potential, including intrinsically nonreciprocal plasmon guiding[25], topological transitions in 2D anisotropic plasmons[22], and directional nanoscale energy collimators[26] (planar and directional light emitter with on-chip integration). However, an experimental observation and verification of them has been elusive so far. Here, we present the first images of in-plane elliptic and hyperbolic polaritons (more precisely, PhPs) that propagate with record-long lifetimes. We found them in thin slabs of α-phase molybdenum trioxide (α-MoO_3), a natural vdWs polar semiconductor. Only recently, phonon polaritons have been observed in α-MoO_3[27], but their anisotropic propagation properties have not been described.

The schematics in Fig. 1a,b show the orthorhombic crystal structure of α-MoO_3, where layers formed by distorted MoO_6 octahedra (Fig. 1a) are weakly bonded by vdWs forces[28] and all three lattice constants (*a*, *b*, and *c*) are different (Fig. 1b). Most important, α-MoO_3 has a strong in-plane structure anisotropy as the difference of the spacing between the (100) and (001) facets is as large as 7.2 %, which will lead to the highly anisotropic response[29] (Supplementary Information). Indeed, the different directional vibrations of the α-MoO_3 crystal structure yield two infrared (IR) "Reststrahlen" bands (RBs)[30] between 800 cm^{-1} and 1000 cm^{-1}, where the typically strong reflectivity between the transverse and longitudinal optical phonon frequencies (TOs and LOs, respectively) shows a large in-plane anisotropy (Supplementary Information). Thus, we can expect that in-plane anisotropic phonon polaritons exist in this material. An optical microscopy image of the α-MoO_3 flakes and their typical Raman spectrum are shown in Fig. 1c, and 1d, respectively. The latter shows characteristic peaks at 820 cm^{-1} and 996 cm^{-1} associated with the lattice vibrations originating the RBs of α-MoO_3.[30]

To explore the polaritonic response of α-MoO_3, we performed polariton interferometry using scattering-type scanning near-field optical microscopy (s-SNOM, Fig. 2a). A vertically oscillating metallized atomic force microscopy (AFM) tip is illuminated with *p*-polarized IR light of wavelength λ_0 and field E_{in} while scanning an α-MoO_3 flake. Acting as an infrared antenna[3-5], the tip concentrates the incident field at the very tip apex to a nanoscale IR spot for local probing of material properties and for exciting polaritons. The tip-scattered radiation is recorded simultaneously with topography, yielding nanoscale resolved near-field images. Specifically, the polaritons (described by the field E and wavelength λ) excited by the tip propagate away and are back-reflected at the flake edges, giving rise to interference fringes with a spacing $\lambda/2$.

Fig.2b shows s-SNOM near-field amplitude images on an α-MoO_3 flake with a thickness d = 250 nm taken at ω = 990 cm^{-1} and ω = 900 cm^{-1}, both frequencies residing inside the two RBs of α-MoO_3[30]. For ω = 990 cm^{-1} (upper image) we observe bright fringes parallel to all the flake edges. They strongly resemble PhPs, similar to what has been observed in s-SNOM experiments with other polar materials[5] and only recently on α-MoO_3[27]. Interestingly, we observe that the fringe periodicity largely depends on the propagation direction, being λ_x = 950 nm and λ_y = 1200 nm for the [100] and [001] crystal directions (Supplementary Information), respectively. Apart from the deep sub-wavelength-scale polariton confinement ($\lambda_{x,y} << \lambda_0$ = 11.1 μm), this finding reveals a strongly anisotropic in-plane propagation (along the flake). This anisotropy becomes even more dramatic at ω = 900 cm^{-1} (lower image), where the fringes are seen only parallel to the [001] direction.

For unambiguous verification of the anisotropic polariton propagation, we recorded spectroscopic line scans[5] (Methods) along the [100] and [001] in-plane crystal directions (Fig. 2c). We observe two spectral bands exhibiting a series of signal maxima (fringes). The band limits (indicated by the horizontal dashed lines) correspond to the transverse and longitudinal optical phonon frequencies of α-MoO_3[30] (denoted by LO_1, LO_2, TO_1 and TO_2) and thus reveal the upper and lower Reststrahlen bands (denoted by U-RB and L-RB). In the U-RB we find that the fringe spacing (corresponding to the polariton wavelength) along both the [100] and [001] directions increases with increasing frequency, indicating a negative phase velocity (analogous to PhPs in the lower Type-I Reststrahlen band of *h*-BN[19]). As in Fig. 2b, we observe a slightly different fringe spacing for the [100] and [001] directions, but now for all frequencies between TO_2 and LO_2. A dramatically different behavior is observed for the L-RB. Along the [100] direction we see fringes whose spacing decreases with increasing frequency, manifesting polaritons with positive phase velocity. More importantly, along the [001] direction we do not observe signal oscillations at a fixed frequency for the whole spectral range between TO_1 and LO_1. This finding indicates the absence of phonon polaritons propagating in the [001] direction, supporting our assumption of a hyperbolic in-plane dispersion. The horizontal fringes observed in Fig. 2c (right panel) are caused by polaritons propagating along the [100] direction. Note that a line profile for a fixed ω corresponds to a vertical line profile (along the [001] direction, respectively parallel to the interference fringes) in the lower panel of Fig. 2b, where we can see that PhPs are launched by the left edge of the flake. Depending on the distance between the tip and the left flake edge (respectively on ω), we thus observe either a constantly bright or dark contrast when the tip is scanned along the [001] direction, corresponding to a bright or dark horizontal fringe in the lower panel of Fig. 2c.

For a better understanding and quantitative analysis of the anisotropic polariton propagation, we extracted the PhPs dispersions, $\omega(k_i)$ ($i = x, y$) from monochromatic s-SNOM images (not shown) of the flake in Fig. 2b. The dispersions for both crystal directions and RBs are plotted in Fig. 2d. For the U-RB (upper panel), the PhPs dispersions along both crystal directions are similar, although slightly separated from each other (*i.e.*, for a same frequency ω, we measured different wavevectors k_i). This result verifies that PhPs in the upper RB propagate with in-plane anisotropy. By plotting the PhPs complex-valued wave-vector we find that the PhPs phase velocity, $v_{p,i} = \omega/k_i$, is negative along both directions, which is indicated by negative k_i values. Furthermore, the remarkably small slopes of the dispersion curves (Supplementary Information) yield unprecedented small group velocities ($v_{g,i} = \frac{\partial k_i}{\partial \omega}^{-1}$) of about $0.8 \times 10^{-3} c$ (at ω = 985 cm^{-1}), which in the future could be exploited for strong light-matter interaction experiments[31]. For the L-RB (lower panel) we only display the PhPs dispersion for the [100] direction, as no PhPs are observed in the orthogonal [001] direction. In this case, the phase velocity is positive (indicated by positive k_x values), and the group velocity is about $0.7 \times 10^{-2} c$ (at ω = 893 cm^{-1}), which is comparable to that of ultraslow PhPs in *h*-BN[11].

To quantify the anisotropy of the PhPs and to measure their iso-frequency contours in the wavevector space, we analyse the PhP propagation along all possible directions on the flake. To that end, we fabricated disks of α-MoO_3 (Methods) and performed polariton interferometry experiments (Supplementary Information) analogous to Fig. 2. Figures 3a and 3b show typical near-field amplitude images taken at frequencies in the U-RB (ω = 983 cm^{-1}) and L-RB (ω= 893 cm^{-1}) of α-MoO_3, respectively. Interestingly, in the U-RB the interference pattern shows an elliptical shape with the largest PhPs wavelength along the [001] surface direction, which continuously reduces to its smallest value along the orthogonal [100] surface direction. More strikingly, in the L-RB the interference pattern manifests as an almond shape, in which the PhPs have the largest wavelength along the [100] direction and continuously reduces to zero until yielding no discernible polariton propagation along the orthogonal [001] direction. By Fourier transform of Figs. 3a and 3b we directly obtain the iso-frequency contours. We find an ellipsoid in the U-RB (Fig. 3c) and hyperbola in the L-RB (Fig. 3d), revealing that the PhPs exhibit elliptic and hyperbolic dispersions, respectively. Note that Fig. 3c shows two ellipses instead of one with a factor of 2 difference in their semi-axes. We attribute this observation to the presence of both tip- and edge-launched PhPs[32,33] in Fig. 3a (Supplementary Information). On the other hand, the hyperbola in Fig. 3d opens along the [001] direction, which indicates that PhPs along this crystal direction are forbidden, thus explaining the observations in Figs. 2 and 3b.

To corroborate our experimental results theoretically, and to extract the yet unknown anisotropic permittivity of α-MoO_3, we model the α-MoO_3 flake as a 2D conductivity layer of zero thickness (Methods). We find the following dispersion relation for polaritons in a thin in-plane anisotropic slab surrounded by two dielectric half-spaces with isotropic permittivities ε_1 and ε_2 (Supplementary Information):

$$\left[k_x^2\alpha_{xx}+k_y^2\alpha_{yy}+\frac{k_0k_t^2}{2}\left(\frac{\varepsilon_1}{k_{z1}}+\frac{\varepsilon_2}{k_{z2}}\right)\right]\left[k_y^2\alpha_{xx}+k_x^2\alpha_{yy}+\frac{k_t^2}{2k_0}(k_{z1}+k_{z2})\right]-k_x^2k_y^2\left(\alpha_{xx}-\alpha_{yy}\right)^2=0$$

(Eq.1)

where $k_{x,y}$, and $k_{z1,2}=\sqrt{\varepsilon_{1,2}k_0^2-k_x^2-k_y^2}$ are the in- and out-of-plane wavevectors, respectively, $k_0=\frac{2\pi}{\lambda_0}$ is the wavevector in free space, and $\hat{\alpha}=2\pi\hat{\sigma}_{\mathrm{eff}}/c$ is the normalized conductivity, introduced for convenience. Using Eq. 1 with α_{xx} and α_{yy} being fit parameters, we obtain excellent agreement (white solid lines) with the elliptical and hyperbolic features in Figs. 3c and 3d. We find α_{xx} = -0.12i (ε_{xx}= 2.6) and α_{yy} = -0.16i (ε_{yy}= 3.7) for ω= 983 cm^{-1} (U-RB), and α_{xx} = 0.26i (ε_{xx}= -6.4) and

α_{yy} = -0.07i (ε_{yy} = 1.7) for ω = 893 cm^{-1} (L-RB).

We corroborate the model and permittivity values by numerical simulations of near-field images of an α-MoO_3 disk on SiO_2. We used the nominal experimental values of 144 nm and 6 μm for the disk thickness and diameter, respectively, and the anisotropic real-valued permittivities obtained from the fit described above. The imaginary parts of the permittivities and the value of ε_{zz} (not obtained from the fit) were adjusted to obtain the best matching of the experimental images and of the sign of the phase velocities in each RB. As a result of our analysis, we find ε_{xx}>0, ε_{yy}>0, and ε_{zz}<0 for the elliptic U-RB, and ε_{xx}<0, ε_{yy}>0, and ε_{zz}>0 for the hyperbolic L-RB (Supplementary Information). The simulated polariton interferometry amplitude images are shown in Figs. 3e and 3f. Their excellent agreement with the experiments (Figs 3a, and 3b) validates both the model and permittivity values. The results demonstrate that experimental PhPs interferometry of α-MoO_3 disks and fitting of the results with our simple theoretical model allows for extracting the highly anisotropic local permittivities of α-MoO_3.

The conductivity tensor $\hat{\sigma}_{\text{eff}}$ - and thus the PhPs wavevector - depends on the slab thickness d. According to the relation between $\hat{\sigma}_{\text{eff}}$ and $\hat{\varepsilon}$ (see above), we obtain from Eq.1 the thickness-dependent anisotropic in-plane polariton wavevectors (Supplementary Information):

$$k_i \approx -\frac{\varepsilon_1+\varepsilon_2}{\mathrm{d}\cdot\varepsilon_{ii}},\ i=x,y \qquad \text{(Eq.2)}$$

In Fig. 4a, we demonstrate the thickness tunability of in-plane hyperbolic polaritons by plotting the PhP dispersions obtained by s-SNOM nano-imaging along the [100] crystal direction of α-MoO_3 flakes with different thickness d. We clearly observe that the wave-vector k_x and thus the polariton confinement increase with decreasing thickness. For d = 55 nm, we find k_x values of about 3.5×10^5 cm^{-1}, corresponding to a PhPs wavelength of 180 nm. This value is 60 times smaller than λ_o = 10.8 μm, suggesting that in-plane anisotropic propagation can be well paired with deep sub-wavelength-scale field confinement for the development of ultra-compact devices. The inverse dependence of k_x on d is better observed in Fig. 4b, where we plot the experimental k_x (red dots) obtained at ω = 902 cm^{-1} for 4 flakes with different thicknesses. These experimental values are well matched by our Eq. 2 (gray curve), where we used ε_{xx}(ω) = -5.1 as extracted for the flake with d = 144 nm in Fig. 3, thus strongly supporting the validity of our approximation.

A key property of polaritons for future applications is their lifetime[10,11]. To measure it we fitted s-SNOM amplitude line profiles along the [100] direction (blue and red crosses in Fig. 4c) with an exponentially decaying sine wave function corrected by the geometrical spreading factor $\sqrt{x}$ (Supplementary Information)[10]. From the amplitude decay length L_x (one of the fitting parameters) we obtain the lifetime according to $\tau_x = L_x/v_g$, where the group velocity v_g is taken from Fig. 2d. For the in-plane hyperbolic PhPs we obtain $\tau_x = 1.9 \pm 0.3$ ps, which reveals the ultra-low-loss character of these polaritons. Surprisingly, for the in-plane elliptic PhPs we obtain $\tau_x = 8 \pm 1$ ps (four times higher than that of PhPs in isotropically enriched *h*-BN[11]). On some flakes we find lifetimes up to 20 ± 4 ps (Supplementary Information). We note that in contrast to low-loss h-BN phonon polaritons[11] and graphene plasmons[12], a rather small amount of fringes were observed on α-MoO_3 flakes. This can be explained by the small group velocities of the MoO_3 PhPs, yielding relatively short propagation lengths. The ultra-long PhP lifetimes are corroborated by the ultra-narrow linewidths of the α-MoO_3 Raman peaks (Supplementary Information) at 996 cm^{-1} and 820 cm^{-1} (corresponding to anisotropic bond stretching modes[30] that originate in the U- and L-RBs, respectively), revealing a very high crystal quality. A similar relation has been recently reported to explain the large lifetimes observed in isotopically enriched *h*-BN[11].

In-plane anisotropic α-MoO_3 PhPs add a unique new member to the growing library of polaritons in vdW materials. In combination with external stimuli, such as strain, electric gating or photo-injection of carriers, we envision the active tuning of the anisotropic PhP properties. Our findings may thus establish a new paradigm in nanophotonics, promising an unprecedented potential for the directional control of light and light-matter interactions at the nanoscale.

(2494 words)

REFERENCES

1 Basov, D., Fogler, M. & de Abajo, F. G. Polaritons in van der Waals materials. *Science* **354**, aag1992 (2016).

2 Low, T. *et al.* Polaritons in layered two-dimensional materials. *Nat. Mater.* **16**, 182 (2016).

3 Fei, Z. *et al*. Gate-tuning of graphene plasmons revealed by infrared nano-imaging. *Nature* **487**, 82-85 (2012).

4 Chen, J. *et al.* Optical nano-imaging of gate-tunable graphene plasmons. *Nature* **487**, 77-81 (2012).

5 Dai, S. *et al.* Tunable phonon polaritons in atomically thin van der Waals crystals of boron nitride. *Science* **343**, 1125-1129 (2014).

6 Chakraborty, S. *et al.* Gain modulation by graphene plasmons in aperiodic lattice lasers. *Science* **351**, 246 (2016).

7 Cai, X. *et al*. Plasmon-enhanced terahertz photodetection in graphene. *Nano Lett.* **15**, 4295-4302 (2015).

8 Rodrigo, D. *et al*. Mid-infrared plasmonic biosensing with graphene. *Science* **349**, 165-168 (2015).

9 Low, T. *et al*. Plasmons and screening in monolayer and multilayer black phosphorus. *Phys. Rev. Lett.* **113**, 106802 (2014).

10 Woessner, A. *et al*. Highly confined low-loss plasmons in graphene–boron nitride heterostructures. *Nat. Mater.* **14**, 421(2014).

11 Giles, A. J. *et al*. Ultralow-loss polaritons in isotopically pure boron nitride. *Nat. Mater.* **17**, 134–139 (2018).

12 Ni, G. X. *et al.* Fundamental limits to graphene plasmonics. *Nature* **557**, 530-533 (2018).

13 Hoffman, A. J. *et al*. Negative refraction in semiconductor metamaterials. *Nat. Mater.* **6**, 946 (2007).

14 Liu, Z., Lee, H., Xiong, Y., Sun, C. & Zhang, X. Far-field optical hyperlens magnifying sub-diffraction-limited objects. *Science* **315**, 1686-1686 (2007).

15 Podolskiy, V. A. & Narimanov, E. E. Strongly anisotropic waveguide as a nonmagnetic left-handed system. *Phys. Rev. B* **71**, 201101 (2005).

16 Cortes, C. L., Newman, W., Molesky, S. & Jacob, Z. Quantum nanophotonics using hyperbolic metamaterials. *J. Opt.* **14**, 063001 (2012).

17 Takayama, O., Bogdanov, A. A. & Lavrinenko, A. V. Photonic surface waves on metamaterial interfaces. *J. .Phy. Condens. Matter* **29**, 463001 (2017).

18 Caldwell, J. D. *et al*. Sub-diffractional volume-confined polaritons in the natural hyperbolic material hexagonal boron nitride. *Nat. Commun.* **5**, 5221 (2014)

19 Yoxall, E. *et al*. Direct observation of ultraslow hyperbolic polariton propagation with negative phase velocity. *Nat. Photon.* **9**, 674 (2015).

20 Li, P. *et al*. Hyperbolic phonon-polaritons in boron nitride for near-field optical

imaging and focusing. *Nat. Commun.* **6**, 7507 (2015).

21 Dai, S. *et al*. Subdiffractional focusing and guiding of polaritonic rays in a natural hyperbolic material. *Nat. Commun.* **6**, 6963 (2015).

22 Gomez-Diaz, J. S., Tymchenko, M. & Alù, A. Hyperbolic Plasmons and Topological Transitions Over Uniaxial Metasurfaces. *Phys. Rev. Lett.* **114**, 233901 (2015).

23 Li, P. *et al.* Infrared hyperbolic metasurface based on nanostructured van der Waals materials. *Science* **359**, 892-896 (2018).

24 Song, J. C. W. & Rudner, M. S. Fermi arc plasmons in Weyl semimetals. *Phys. Rev. B* **96**, 205443 (2017).

25 Mazor, Y. & Steinberg, B. Z. Longitudinal chirality, enhanced nonreciprocity, and nanoscale planar one-way plasmonic guiding. *Phys. Rev. B* **86**, 045120 (2012).

26 Kildishev, A. V., Boltasseva, A. & Shalaev, V. M. Planar Photonics with Metasurfaces. *Science* **339**, 1232009 (2013).

27 Zheng, Z. *et al*. Highly confined and tunable hyperbolic phonon polaritons in van der Waals semiconducting transition metal oxides. *Adv. Mater.* **30**, 1705318 (2018).

28 de Castro, I. A. *et al*. Molybdenum Oxides - From Fundamentals to Functionality. *Adv. Mater.* **29**, 1701619 (2017).

29 Lajaunie, L., Boucher, F., Dessapt, R. & Moreau, P. Strong anisotropic influence of local-field effects on the dielectric response of α-MoO_3. *Phys. Rev. B* **88**, 115141 (2013).

30 Py, M. A., Schmid, P. E. & Vallin, J. T. Raman scattering and structural properties of MoO_3. *IL Nuovo Cimento B* **38**, 271-279 (1977).

31 Caldwell, J. D. *et al*. Low-loss, infrared and terahertz nanophotonics using surface phonon polaritons. *Nanophotonics* **4**, 44-68 (2015).

32 Dai, S. *et al*. Efficiency of launching highly confined polaritons by infrared light incident on a hyperbolic material. *Nano Lett.* **17**, 5285–5290 (2017).

33 Hu, F. *et al*. Imaging the localized plasmon resonance modes in graphene nanoribbons. *Nano Lett.* **17**, 5423–5428 (2017).

Acknowledgements

We thank S. C. Dhanabalan and J. S. Ponraj for their efforts at the early stage of this project. We thank M. H. Lu, L. Liu, C. W. Qiu and L. Wang for constructive suggestions, H. Yan and Q. Xing for the assistance on micro-FTIR measurements. We thank Quantum Design China (Beijing lab) for the technical support on part of s-SNOM measurements. This work was performed in part at the Melbourne Centre for Nanofabrication (MCN) in the Victorian Node of the Australian National Fabrication Facility (ANFF). We acknowledge the support from the National Natural Science Foundation of China (No. 51222208, 51290273, 51601131, 61604102 51702219 and 91433107), the National Key Research & Development Program (No. 2016YFA0201900), ARC (DP140101501, IH150100006, FT150100450 and CE170100039), the Natural Science Foundation of Jiangsu Province (No. BK20150053), the Priority Academic Program Development of Jiangsu Higher Education Institutions (PAPD) and Collaborative Innovation Center of Suzhou Nano Science and Technology, the Spanish Ministry of Economy, Industry and Competitiveness (national projects MAT2015-65525-R, FIS2014-60195-JIN, MAT2017-88358-C3-3-R, MAT2014-53432-C5-4-R, and the project MDM-2016-0618 of the Maria de Maeztu Units of Excellence Programme). Q. Bao acknowledges the support from the Australian Research Council (ARC) Centre of Excellence in Future Low-Energy Electronics Technologies (FLEET). P. Alonso-González acknowledges the support from the European Research Council under the Starting grant 715496, 2DNANOPTICA. J.M-S acknowledges support through the Clarín Programme from the Government of the Principality of Asturias and the Marie Curie-COFUND actions (PA-18-ACB17-29). P.L acknowledges the support from the Marie Sklodowska-Cuire individual fellowship (SGPCM-705960).

Author contributions

W.M. P.A-G. and S.L. contributed equally to this work. Q.B. conceived the original concept. R.H., P.A-G. and Q.B. supervised the project. W.M. and P.A-G. Z.D. carried out the near-field imaging experiments with the help of I.A, J.M-S, J.T-G, and P.L. J.Y carried out the far-field experiments. W.M., P.A-G., A.Y.N, S.L., R.H, and Q.B. participated in data analysis and co-wrote the manuscript. A.Y.N. suggested the model and supervised the theory. J.M-S, J.T-G and P.A-G. carried out the simulations. Y.J., S.S., Y.Z. and K.K-Z. contributed to the material synthesis. S.V. C.T. Z.D. and Y.Z. contributed to sample fabrication.

Competing interests

R.H. is cofounder of Neaspec GmbH, a company producing scattering-type near-field scanning optical microscope systems, such as the one used in this study. The remaining authors declare no competing financial interests.

Additional information

Supplementary Information is linked to the online version of the paper.

Reprints and permissions information is available online at www.nature.com/reprints.

Correspondence and requests for materials should be addressed to (P.A.G.) pabloalonso@uniovi.es, (R.H.) r.hillenbrand@nanogune.eu and (Q.B.) qiaoliang.bao@monash.edu

All the data is available in the online version of the paper.

Main figure legends

Fig. 1 | Physical properties of α-MoO_3.
a, Illustration of the orthorhombic lattice structure of layered α-MoO_3 (red spheres: oxygen atoms). The orthorhombic structure is based on bilayers of distorted MoO_6 octahedra and stacked along the [010] direction via van der Waals interactions. **b,** Schematics of the unit cell of α-MoO_3, the lattice constants are a=0.396 nm, b=1.385 nm, and c=0.369 nm. **c**, Optical image of α-MoO_3 flakes. The α-MoO_3 crystals typically appear to be rectangular due to the anisotropic crystal structure. The arrows indicate the crystal directions. Scale bars: 20 µm. **d**, Raman spectrum taken in the area marked by a red dashed circle in c.

Fig. 2 | Real-space imaging and nano-spectroscopy of an α-MoO_3 flake.
a, Schematics of the s-SNOM experimental configuration used to image an α-MoO_3 flake. A metalized AFM tip illuminated by *p*-polarized IR light detects the back-scattered near fields. **b,** Near-field amplitude images of an α-MoO_3 flake with thickness d = 250 nm at illuminating frequencies ω = 990 cm^{-1}, and ω = 900 cm^{-1}. Scale bars: 2 µm. **c,** Bottom row: Nano-FTIR spectral line scans along [100] and [001] (white lines in b). The dashed lines are guides to the eyes for the maxima in the U-RB. Dashed lines mark the longitudinal and transversal phonon modes in α-MoO_3 (TO_1: 820 cm^{-1}; LO_1/ TO_2: 960 cm^{-1}; LO_2: 1000 cm^{-1}). Top row: Zooms into the areas of the U-RB that are marked by black rectangles in the bottom row. **d,** PhPs dispersion along the [100] and [001] directions in the U-RB (Upper panel) and L-RB (Lower panel). Gray lines in both panels are guides-to-the-eye obtained by fitting.

Fig. 3 | In-plane elliptical and hyperbolic PhPs in an α-MoO_3 disk.
a, b, Near-field amplitude images of an α-MoO_3 disk (in color) with d = 144 nm. The imaging frequencies are ω = 983 cm^{-1} (U-RB), and 893 cm^{-1} (L-RB). Dashed white lines indicate the [100] and [001] surface directions. Scale bars: 2 µm. **c, d,** Absolute value of the Fourier transform of the near fields in a and b revealing the isofrequency contours for each RB. Solid lines show the PhPs isofrequency contours obtained by fitting Eq. 1 for each case (note that they correspond to $2k_p$). **e, f,** Calculated near-field amplitude images for an α-MoO_3 disk at ω = 983 cm^{-1} (U-RB), and 893 cm^{-1} (L-RB), respectively. Scale bars: 2 µm.

Fig. 4 | Thickness tunability and lifetime of in-plane hyperbolic and elliptic PhPs in α-MoO_3.
a, Experimental (dots) PhPs dispersions along the [100] direction in α-MoO_3 for a varying flake thickness d (lines are guides to the eyes). **b,** Experimental (dots) and

calculated (line) dependence of k_x upon d. **c,** s-SNOM line traces along the [100] direction of the flake shown in Fig. 2b with d = 250 nm in the elliptic (blue crosses, ω = 990 cm^{-1}) and hyperbolic regimes (red crosses, ω = 930 cm^{-1}). Fits to a damped sine wave function are shown as black solid lines.

METHODS

s-SNOM and nanoFTIR set-up.

For infrared nano-imaging we used a scattering-type scanning near-field optical microscope (s-SNOM[3-5]) from Neaspec GmbH where a metallized AFM tip oscillating at its resonant frequency (270 kHz) with a tapping amplitude of about 50 nm is illuminated along its long axis (E_z) with IR light of frequency ν_0 (from tunable CO_2 and Quantum Cascade lasers) while it raster scans an α-MoO_3 flake. As an infrared antenna, the Pt-coated tip concentrates the incident field into a nanoscale spot at the apex. In the particular case of probing a material supporting polaritons, this nanoscale 'hot spot' acts as a local source and detector of polaritons[3-5], thus revealing interferometric (interference of forward- and backward-propagating polaritons) near-field images where the distance between adjacent maxima corresponds to half the polariton wavelength, $\lambda_p/2$. The polariton back-scattered near fields are imaged and spectrally analyzed by recording the tip-scattered field with a pseudo-heterodyne Michelson interferometer[34] as a function of tip position, yielding near-field images (Fig. 2b) that are demodulated at the 3rd and 4th harmonic of the tip vibration frequency.

For nano-FTIR spectroscopy[35], the tip was illuminated by a broadband super-continuum laser, and the tip-scattered light was recorded with an asymmetric Fourier transform spectrometer. By recording point spectra as a function of the tip position, we obtained high-resolution spectral line scans[5].

Disks fabrication.

Bulk MoO_3 crystals were grown via chemical vapor deposition. Commercial MoO_3 powder (Sigma-Aldrich) was evaporated in a horizontal tube furnace at 785 °C and was re-deposited as α-MoO_3 crystals at 560°C. The deposition process was carried out in an inert environment (Ar flow of 200 sccm) at 1 Torr.[28] The as-grown bulk crystals were then mechanically exfoliated and transferred onto a Si/SiO_2 (thickness: 300 nm) substrate. The transferred flakes were inspected with an optical microscope and characterized via AFM, allowing the selection of large and homogeneous pieces with the desired thickness. The selected flake was then shaped into a disk by using focused Ga-ion beam milling in a FEI Helios 600 Nanolab dual beam system. In order to protect the surface of the disk from the implantation of Ga ions, the flake was first fully covered by a thin (thickness: 500 nm) diamond mask. To do this the tungsten tip of an Omniprobe micromanipulator was attached to a diamond film using an *in situ* platinum deposition. The diamond mask was cut free from the bulk diamond film, and then manually placed onto the surface of the flake. Subsequently both the flake and the diamond mask were etched away in a ring pattern all the way through to the substrate using the ion beam. The outer mask, still attached to the Omni probe, was then lifted away and cut off the Omniprobe tip with the ion beam. The Omniprobe was then reattached to the central diamond disk by a small electron beam platinum deposition, and it too was lifted off the surface to give the disc shaped flake separated from the bulk flake by a ring-shaped channel.

Conductivity model for MoO_3 layers.

Modelling the α-MoO_3 flake as a 2D conductivity layer of zero thickness avoids the calculation of the fields inside the slab[22], and has been proven valid for in-plane isotropic 2D materials (*e.g.*, graphene[36] and transition layer polaritons[37]) with a layer thickness that is much smaller than the polariton wavelength ($d << \lambda$). In the model, the effective conductivity is given by $\sigma_{\text{eff}} = (c\text{d}/2i\lambda_0)\,\varepsilon$, where ε is the in-plane isotropic permittivity (both ε and σ_{eff} are scalars). Note that σ_{eff} scales linearly with d, thus taking into account the effect of the small slab thickness. Analogously, we model the α-MoO_3 layer by an anisotropic in-plane conducting layer with zero thickness and an effective two-dimensional conductivity tensor, $\hat{\sigma}_{\text{eff}}$. The generalized relation between the tensor $\hat{\sigma}_{\text{eff}}$ and the (2×2) permittivity tensor $\hat{\varepsilon} = \text{diag}(\varepsilon_{xx}, \varepsilon_{yy})$ is then given by $\hat{\sigma}_{\text{eff}} = (c\text{d}/2i\lambda_0)\hat{\varepsilon}$. Note that the model is independent of the out-of-plane permittivity component ε_{zz}, which subsequently does not enter into the equation.

METHODS REFERENCES

34 Ocelic, N., Huber, A. & Hillenbrand, R. Pseudoheterodyne detection for background-free near-field spectroscopy. *Appl. Phys. Lett.* **89**, 101124 (2006).

35 Huth, F., Schnell, M., Wittborn, J., Ocelic, N. & Hillenbrand, R. Infrared-spectroscopic nanoimaging with a thermal source. *Nat. Mater.* **10**, 352 (2011).

36 Nikitin, A. Y. in World Scientific Handbook of Metamaterials and Plasmonics *World Scientific Series in Nanoscience and Nanotechnology* 307-338 (World Scientific, 2017).

37 Tilley, D. R. Surface Polaritons: Electromagnetic Waves at Surfaces and Interfaces. (North-Holland Pub. Co, 1982).

Data availability

The data that support the findings of this study are available from the corresponding author on reasonable request.

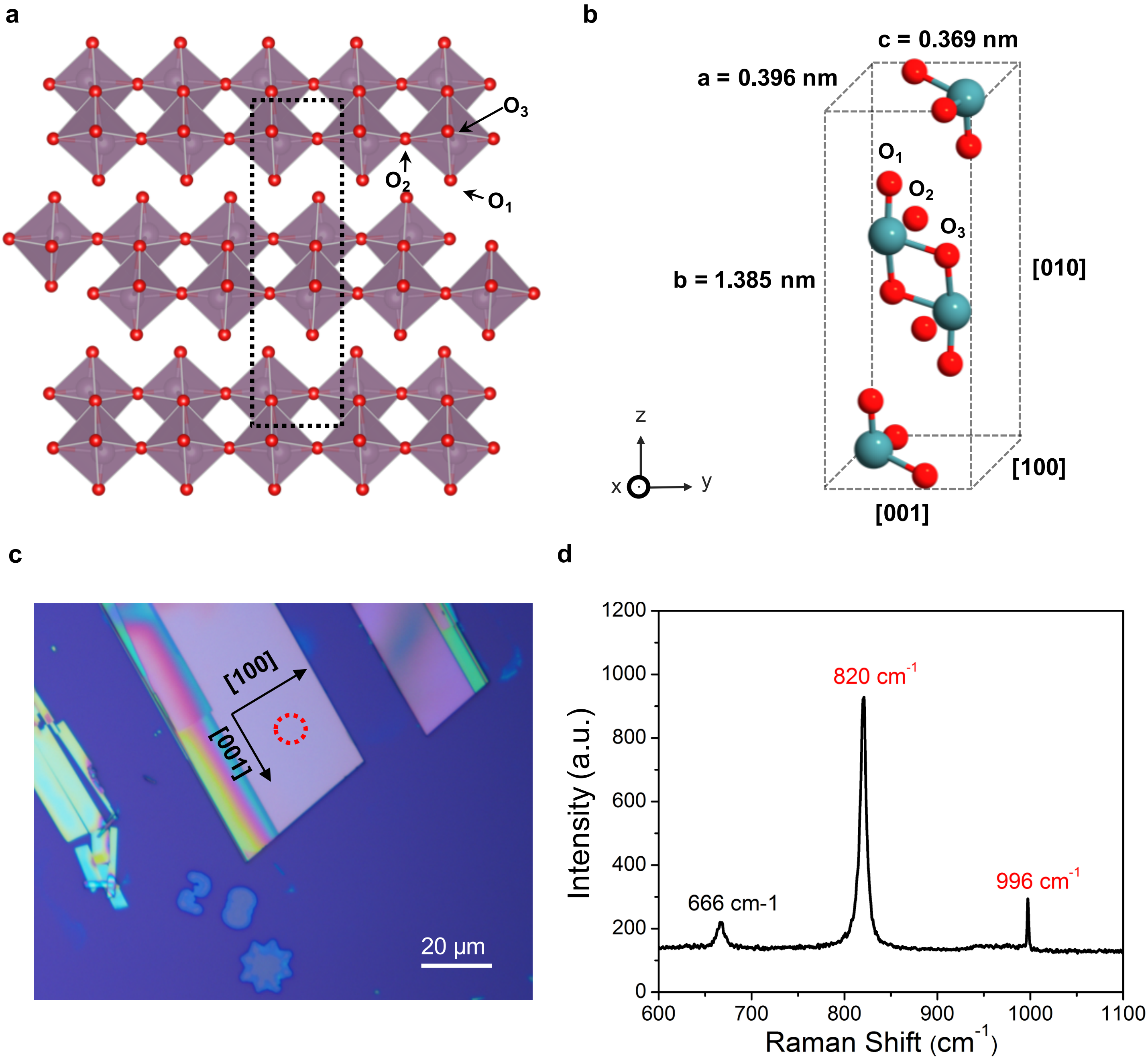
a
O_3
O_2
O_1
b
c = 0.369 nm
a = 0.396 nm
b = 1.385 nm
O_1
O_2
O_3
[010]
[100]
[001]
z
x
y
c
[100]
[001]
20 μm
d
Intensity (a.u.)
Raman Shift (cm^{-1})
666 cm-1
820 cm^{-1}
996 cm^{-1}
0
200
400
600
800
1000
1200
600
700
800
900
1000
1100

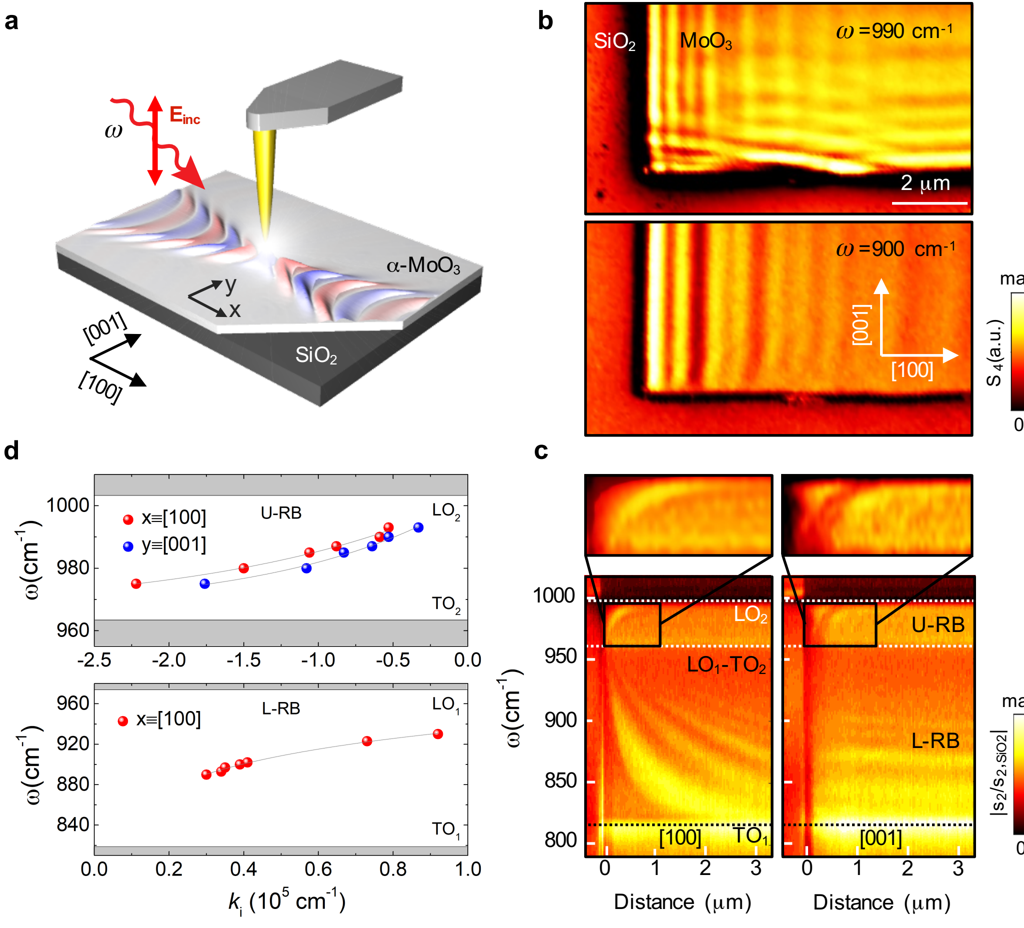

a
ω
E_inc
α-MoO3
y
x
[001]
[100]
SiO2
b
SiO2
MoO3
ω =990 cm-1
2 μm
ω =900 cm-1
[001]
[100]
max
S4(a.u.)
0
d
ω(cm-1)
1000
980
960
x≡[100]
y≡[001]
U-RB
LO2
TO2
-2.5
-2.0
-1.5
-1.0
-0.5
0.0
960
920
880
840
x≡[100]
L-RB
LO1
TO1
0.0
0.2
0.4
0.6
0.8
1.0
ki (10^5 cm-1)
c
1000
950
900
850
800
ω(cm-1)
LO2
LO1-TO2
[100]
TO1
U-RB
L-RB
[001]
0
1
2
3
Distance (μm)
max
|s2/s2,SiO2|
0

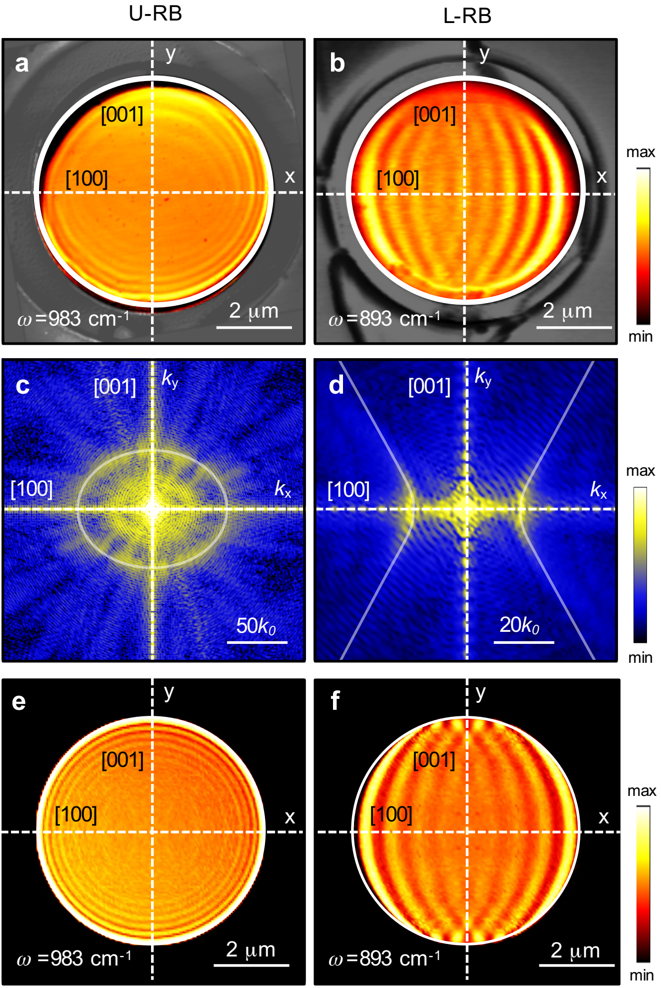

U-RB
L-RB
a
b
c
d
e
f
[001]
[100]
x
y
k_x
k_y
ω=983 cm^{-1}
ω=893 cm^{-1}
2 μm
$50k_0$
$20k_0$
max
min

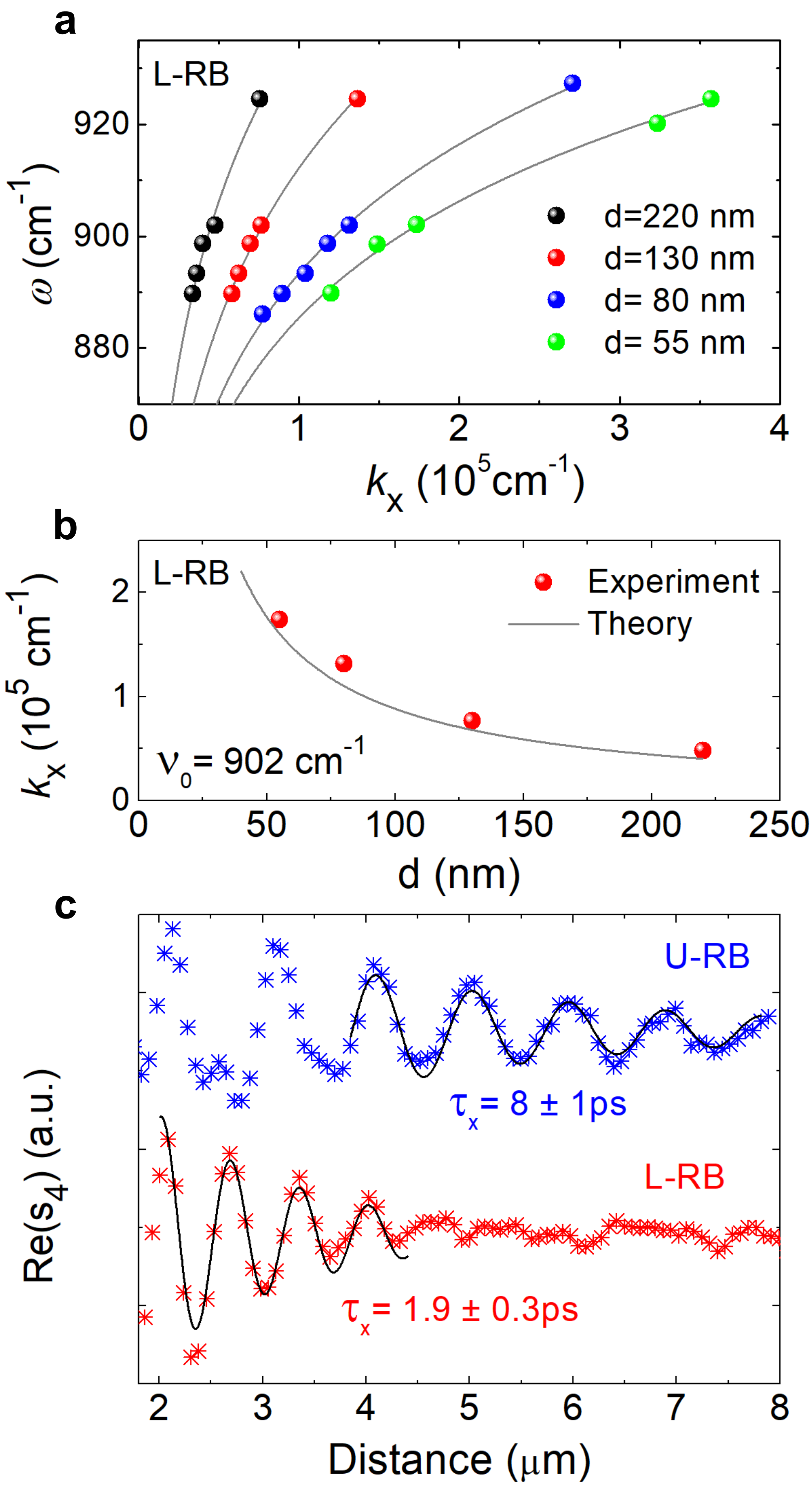

a
L-RB
d=220 nm
d=130 nm
d= 80 nm
d= 55 nm
ω (cm^-1)
k_x (10^5 cm^-1)
b
L-RB
Experiment
Theory
ν_0= 902 cm^-1
k_x (10^5 cm^-1)
d (nm)
c
U-RB
τ_x = 8 ± 1ps
L-RB
τ_x = 1.9 ± 0.3ps
Re(s_4) (a.u.)
Distance (μm)